

Operando X-ray Diffraction Characterization for Understanding the Intrinsic Electrochemical Mechanism in Rechargeable Battery Materials

Xiujuan Wei, Xuanpeng Wang, Qinyou An, Chunhua Han,* and Liqiang Mai*

Studying and understanding the physical and chemical changes in electrode materials during cycling is important for achieving high-performance rechargeable batteries. Operando X-ray diffraction (XRD), as an efficient analytic method, has been developed to probe the phase transitions and crystal-structure changes in electrodes. Recent progress in studying the electrochemical reaction process of electrodes during cycling by the operando XRD analysis method is summarized. The applications of operando XRD toward both cathode and anode materials of rechargeable batteries are summarized, including polyanionic compounds, layered oxides, and insertion-, conversion- and alloying-type anodes. The correlation between the structure changes and electrochemical performance of electrode materials is systematically analyzed. Finally, the challenges and perspectives on the development of the operando XRD characterization method in electrode materials are introduced and discussed.

1. Introduction

To settle the global environmental issues and integrate renewable energy sources into the smart grid, the development of energy-storage devices has become more and more important. Among the different kinds of energy-storage devices, rechargeable batteries as efficient electrochemical-energy-storage devices have drawn great attention.^[1] For instance, lithium-ion batteries (LIBs) have been widely used in portable electronic devices, owing to their high energy density and environmental benignity. Recently, sodium-ion batteries (SIBs) have also attracted a great deal of attention and are considered as a potential substitute to LIBs because of their low cost and the abundant

resources of sodium.^[2] In modern society, rechargeable batteries play a vital role due to their efficient electrical energy storage. In order to meet the increasing demands for portable electronic devices, electric vehicles (EV), and grid-storage systems, the development of high-performance rechargeable batteries is urgently desired. Many research studies have been devoted to enhancing the electrochemical properties of electrode materials, achieving high-energy- and high-power-density rechargeable batteries.^[3–5] However, a fundamental understanding of the intrinsic limitations of electrode materials is still unclear.

The electrode materials, as an important component of batteries, play a critical role in defining the overall performance of a rechargeable battery. During the

charge/discharge reaction process, various physical and chemical changes will occur in electrode materials, such as lattice evolution, phase transitions, and structural degradation. These changes affect the electrochemical performance of rechargeable batteries to some extent. Thus, it is necessary to detect these physical and chemical processes during cycling, in order to optimize and enhance the electrochemical performance of electrode materials. Numerous researchers have studied the electrochemical storage mechanism and the crystal-structure changes in electrode materials based on ex situ methods, such as X-ray diffraction (XRD),^[6,7] X-ray photoelectron spectroscopy (XPS),^[8] and transmission electron microscopy (TEM).^[9] However, when the electrode materials are removed from the cells and exposed to air, the surface properties of the electrodes will be changed, affecting the characterization and observation of the electrochemical processes. To avoid these drawbacks, operando analytic methods are exploited. Kim et al.^[10] studied the phase stability of binary Fe and Mn olivine materials using temperature-controlled operando XRD and identified that the Fe/Mn ratio affects the thermal behavior of partially charged olivine materials. Zhao et al.^[11] performed operando TEM characterization to investigate the stabilizing effect and self-adaptive behavior of crumpled grapheme. Hua et al.^[12] investigated the reaction mechanisms of CuF₂ via an array of characterization methods. Based on operando X-ray absorption near-edge structure (XANES) spectroscopy and cyclic-voltammetry results, it is revealed that Cu directly forms during the first discharge and an intermediate Cu(I) species forms during the first charge. Mai et al.^[13] designed

X. J. Wei, X. P. Wang, Prof. Q. Y. An, Prof. C. H. Han, Prof. L. Q. Mai
State Key Laboratory of Advanced Technology for
Materials Synthesis and Processing
International School of Materials Science and Engineering
Wuhan University of Technology
Wuhan 430070, P. R. China
E-mail: hch5927@whut.edu.cn; mlq518@whut.edu.cn

Prof. L. Q. Mai
Department of Chemistry
University of California
Berkeley, California 94720, USA

 The ORCID identification number(s) for the author(s) of this article can be found under <http://dx.doi.org/10.1002/smt.201700083>.

DOI: 10.1002/smt.201700083

a single-nanowire-electrode device for operando probing the intrinsic reason for the electrode capacity fading and revealing the structure change at the single-nanowire level by confocal Raman microscopy. These operando techniques realize the effective observation of the dynamic electrochemical process in the working state of electrode materials. Among these operando analyses, the operando XRD technique is considered to be an important analytic tool, identifying phase transitions, lattice constant changes, and crystal evolutions (**Figure 1**). These changes are closely related to the electrochemical processes of electrodes during charge/discharge. For instance, the phase transformation is usually caused by redox reaction in the electrodes. Lee et al.^[14] performed operando XRD to investigate the structural evolution of lithium-excess nickel titanium molybdenum oxides upon charge/discharge. On the basis of characterization results from the operando XRD, XANES spectroscopy, electron energy-loss spectroscopy, and electrochemistry, it is proposed that the first charge of $\text{Li}_{1.2}\text{Ni}_{1/3}\text{Ti}_{1/3}\text{Mo}_{2/15}\text{O}_2$ to 4.8 V is accompanied by $\text{Ni}^{2+}/\text{Ni}^{3+}$ oxidation, oxygen loss, and oxygen oxidation largely in this sequence, after which Mo^{6+} and/or Ti^{4+} can be reduced upon discharge. Nelson et al.^[15] studied the structural and morphological changes in Li-S batteries by operando XRD and transmission X-ray microscopy. It was proven that the recrystallization of sulfur by the end of the charge cycle is dependent on the preparation technique of the sulfur cathode. The crystalline Li_2S does not form at the end of discharge for all the sulfur cathodes studied. Wu et al.^[16] investigated the structural evolution of Na_xTiO_2 upon electrochemical de-intercalation by operando XRD. The results revealed a reversible $\text{O}3\text{-O}'3$ phase transition, including an unusual lattice parameter variation coupled to complicated Na vacancy orderings in a series of second-order phase transitions. Wang et al.^[17] performed synchrotron-based operando transmission X-ray microscopy and high-energy XRD,

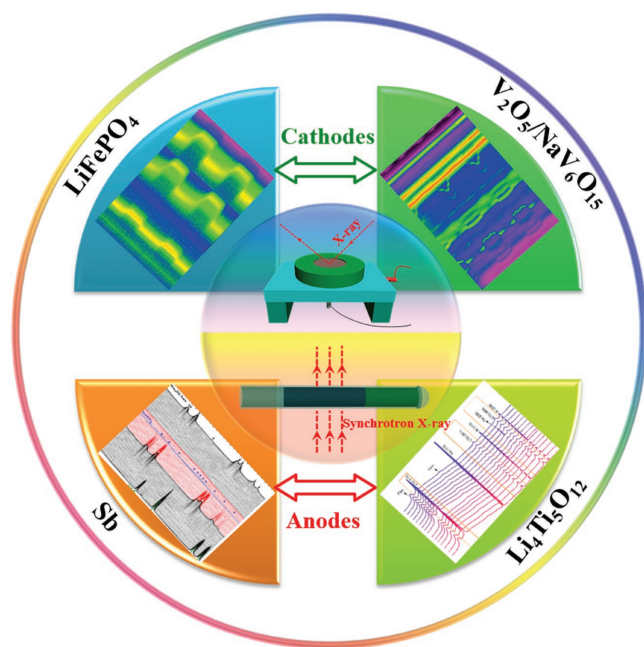


Figure 1. Schematic of the operando XRD characterization for electrode materials in rechargeable batteries.



Xiujuan Wei received her B.S. degree from the Department of Material and Chemical Engineering at Zhengzhou University of Light Industry in 2013. She is working toward her Ph.D. degree at Wuhan University of Technology. Her current research involves operando analysis techniques and transitional-metal chalcogenides for rechargeable batteries.



Chunhua Han is an Associate Professor of Materials Science and Engineering at Wuhan University of Technology (WUT). She received her M.S. degree in material science from WUT in 2006, and her Ph.D. degree from WUT in 2013. Her current research focuses on energy-storage materials and devices.



Liqiang Mai is a Cheung Kong Scholar Chair Professor at Wuhan University of Technology (WUT). He received his Ph.D. degree from WUT in 2004 and carried out his postdoctoral research in Prof. Zhonglin Wang's group at Georgia Institute of Technology (2006–2007). He worked as an advanced research scholar in

Prof. Charles M. Lieber's group at Harvard University (2008–2011) and Prof. Peidong Yang's group at University of California, Berkeley (2017). His research interests focus on nanowire materials and devices for energy storage.

and clarified the dissymmetric phase transformation and structure-evolution mechanism of layered NaNiO_2 material. It was confirmed that the phase transformation and deformation of NaNiO_2 during the voltage range of below 3.0 V to over 4.0 V are responsible for the irreversible capacity loss during the first cycling. The clear observation of the real-time electrochemical process and reaction mechanism makes it easy to understand the factors influencing the degradation of electrode materials. Thus, in order to design and fabricate high-performance electrode materials, many researchers have focused on testing and analyzing the chemical and physical changes through the operando XRD technique.

Table 1. Classification of the electrode materials by operando XRD characterization in rechargeable batteries.

Classification		Materials	Energy-Storage Systems	Analytical Viewpoint
Cathode Materials	Polyanionic Compounds	LiFePO ₄ ^[26,27]	LIBs	Phase transition
		LiMn _{0.25} Fe _{0.75} PO ₄ ^[37]	LIBs	Phase transition
		Na ₃ V ₂ (PO ₄) ₃ ^[35]	NIBs	Structure evolution
		K ₃ V ₂ (PO ₄) ₃ ^[36]	NIBs	Structure evolution
	Layered Oxides	NaNiO ₂ ^[17]	NIBs	Phase transition
		V ₂ O ₅ /NaV ₆ O ₁₅ ^[44]	LIBs	Phase transition
		P2-Na _x CoO ₂ ^[50]	NIBs	Phase transition
		Na _{0.7} Fe _{0.5} Mn _{0.5} O ₂ ^[38]	NIBs	Structure evolution
		K _{0.7} Fe _{0.5} Mn _{0.5} O ₂ ^[47]	KIBs	Structure evolution
		Anode Materials	Insertion Type	NaTiO ₂ ^[16]
Li ₄ Ti ₅ O ₁₂ ^[55]	NIBs			Reaction mechanism
Na ₃ Ti ₂ (PO ₄) ₃ ^[30]	NIBs			Structure evolution
Conversion Type	Mn ₃ O ₄ ^[59]		LIBs	Phase transition
	Fe ₃ O ₄ /VO _x /G ^[64]		LIBs	Structure evolution
	Co ₂ V ₂ O ₇ ^[66]		LIBs	Reaction mechanism
Alloying Type	Si ^[73]		LIBs	Reaction mechanism
	Sb ^[78]		NIBs	Reaction mechanism

Here, we summarize the recent research progress on the characterization of rechargeable-battery electrodes by the operando XRD method. The application and development of the operando XRD characterization method in both cathode and anode materials for rechargeable batteries are listed (see Table 1) and discussed in this review, including polyanionic compounds, layered oxides, and insertion-, conversion-, and alloying-type anodes. Moreover, the intrinsic reason of the electrochemical performance degradation and fundamental understanding of the structural changes are also analyzed in detail, which is helpful in exploring and designing next-generation electrode materials.

2. Operando XRD Technique for Cathode Materials

2.1. Polyanionic Compounds

2.1.1. Observation on the Phase Evolution of LiFePO₄

Since Goodenough and co-workers^[18] reported LiFePO₄ as a positive electrode material for LIBs, LiFePO₄ has attracted great interest and is now considered as one of the most promising cathode material for LIBs, owing to its high thermal stability, low cost, environmental friendliness, and safe properties. During cycling, electrochemical delithiation/lithiation proceeds through a two-phase reaction process between LiFePO₄ and FePO₄. However, the poor ionic and electronic conductors of end-member phases hinder the fast Li⁺ insertion/extraction in LiFePO₄. To make this electrode material meet the demand for high-performance large-scale application in

EVs, numerous studies have been carried out to optimize and investigate the reaction mechanism of LiFePO₄.^[19–22] Some strategies have been adopted to improve the rate performance of LiFePO₄, such as reducing the particle size^[23] and mixing with carbon materials.^[24] Modifying the electrochemical performance relies highly on understanding the phase-transformation mechanisms and ion-diffusion kinetics of the electrode materials. The development of operando methods is required to elucidate the phase-transition behavior through real-time observation. Recently, Orikasa et al.^[25] investigated the phase transition of LiFePO₄ under battery operation using time-resolved XRD. It was revealed that a metastable crystal phase transiently emerges between LiFePO₄ and FePO₄, and the phase-transition path passes through the metastable phase, accounting for the high rate capability of LiFePO₄. Liu et al.^[26] used a dilute electrode and time-resolved operando XRD to probe the phase-transformation process of LiFePO₄. The existence of a facile non-equilibrium single-phase-transformation pathway can explain the high rate performance of LiFePO₄. Despite the great

progress in studying the electrochemical performance and phase-transition behavior of LiFePO₄ at room temperature that has been achieved, a breakthrough in its low-temperature performance and probing the phase-transformation process at low temperature is still needed.

Yan et al.^[27] investigated the phase-transformation routes of LiFePO₄/FePO₄ at different cyclic voltammetry (CV) scan rates and temperatures by operando two-dimensional XRD (XRD²) with laboratory XRD. An electrochemical-cell module with an X-ray-transparent beryllium window was used, while the slurry was directly cast on the beryllium window. The cell was assembled in an argon-filled glove box. During the charge/discharge process, the operando XRD signals were collected directly using a planar detector. The results revealed the existence of intermediate phases during the lithium insertion/extraction processes at low temperature. Figure 2a–c show operando diffraction patterns of LiFePO₄ at various scan rates at 1.4, 2.8 and 4.2 mV s⁻¹ at 293 K. It can be observed that the continuous positive intensities appear in the 2θ range between 41.7° and 42.8° in the selected diffraction patterns at a scan rate of 4.2 mV s⁻¹ (Figure 2c). This phenomenon reveals the possible existence of intermediate phases between LiFePO₄ and FePO₄ under a thermodynamic equilibrium state. The phase-transition processes of LiFePO₄ were also probed by operando XRD² at scan rates of 1.4, 2.8, and 4.2 mV s⁻¹ at a low temperature of 273 K, as shown in Figure 2d–f. It was observed that the (211), (311), and (121) reflections become broad asymmetrically with the charge proceeding, which is accompanied by the formation of intermediate phases. In addition, the selected diffraction peaks shift to higher angle after cycling, indicating a decrease of the unit-cell volume. Figure 3a–c show the ion-diffusion coefficients and structure evolution of LiFePO₄ at different temperatures. With

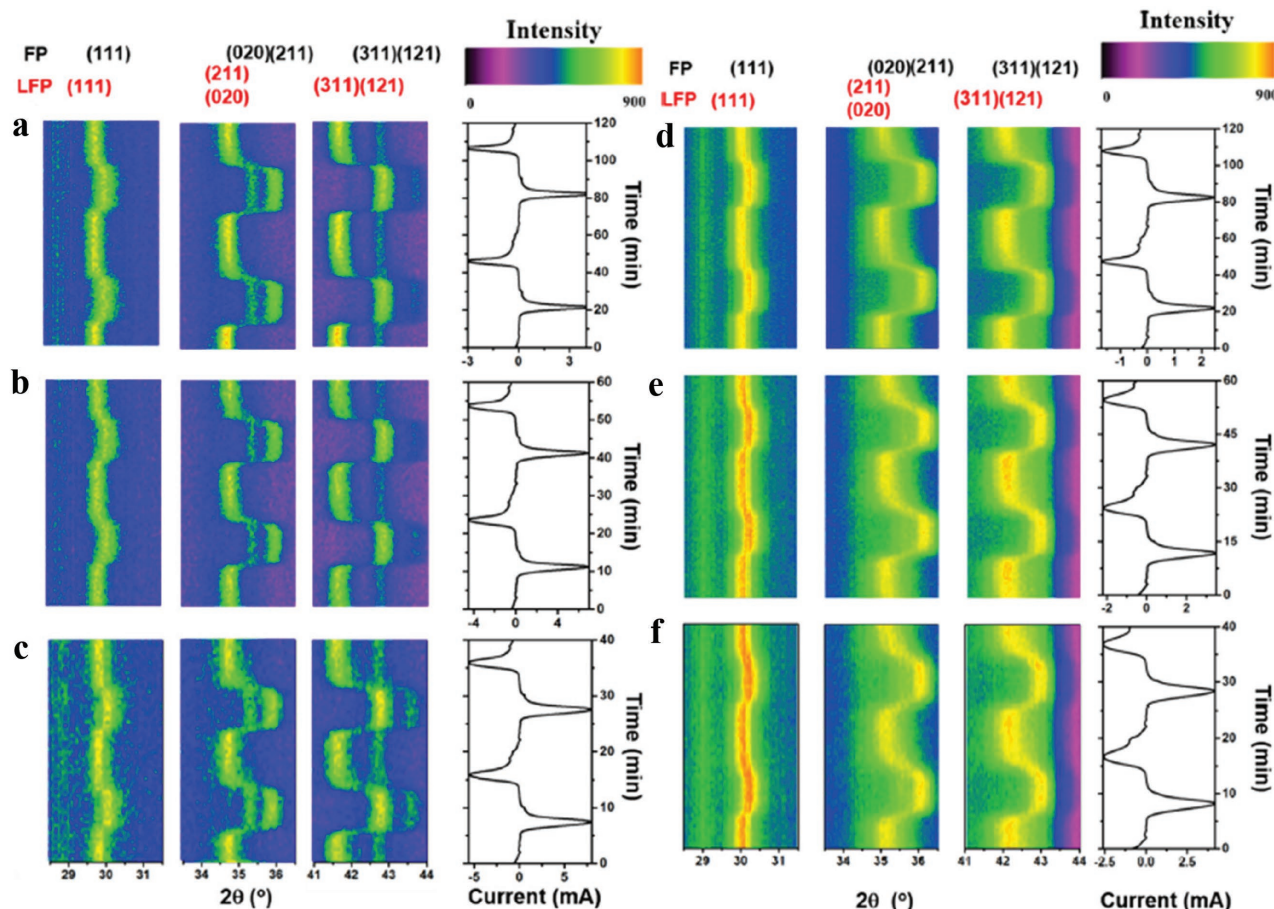


Figure 2. The image plot of diffraction patterns for (111), (211), (020), (311), and (121) reflections during the two CV cycles under different scan rates of 1.4 (a,d), 2.8 (b,e), and 4.2 mV s^{-1} (c,f) at temperatures of 293K (a–c) and 273 K (d–f). The corresponding current curves are plotted on the right. LFP represents LiFePO_4 ; FP represents FePO_4 . a–f) Reproduced with permission.^[27] Copyright 2016, Elsevier.

the temperature reducing from 293 to 273 K, the ion-diffusion coefficient decreases slightly, as shown in Figure 3a. This demonstrates that the formation of intermediate phases can alleviate the kinetic limitation of LiFePO_4 . The lattice-parameter variations are confirmed, as shown in Figure 3b,c. When cycling at a temperature of 273 K, it is found that the parameter b decreases and increases with time in the cathodic and anodic reaction processes, respectively. These results indicate a solid-solution reaction between LiFePO_4 and FePO_4 .

The intermediate phases of LiFePO_4 were captured by the operando XRD² analysis method at a relatively low temperature. The appearance of intermediate phases can inhibit the degradation of the ion-diffusion coefficient at low temperature. Such a high-time-resolution operando XRD² analysis method can also be applied to observe the processes during the reaction time of other rechargeable battery electrodes.

2.1.2. Studying the Electrochemical Reaction Process of $\text{Na}_3\text{V}_2(\text{PO}_4)_3$

In the past decade, sodium super ionic conductor (NASICON)-structured compounds derived from the polyanion system have

been widely studied as potential cathodes for SIBs, which possess an open framework containing large interstitial channels and provide high ionic mobility.^[28–32]

As a typical NASICON-structured compound, $\text{Na}_3\text{V}_2(\text{PO}_4)_3$ has received extensive attention in SIBs owing to the highly covalent three-dimensional open frameworks, which provide high ionic conductivity and large interspace.^[33,34] Although $\text{Na}_3\text{V}_2(\text{PO}_4)_3$ has been considered as one of the best candidates for room-temperature SIBs. However, its intrinsic sodium-storage mechanism and the crystal-structure evolution during the charge/discharge processes are still unclear. Ren et al.^[35] reported a novel three-dimensional $\text{Na}_3\text{V}_2(\text{PO}_4)_3$ nanofiber network controllably constructed via a facile self-sacrificed template method. The crystal-structure evolution during the sodium-ion insertion/extraction processes was investigated through the operando XRD technique with laboratory XRD (Figure 3d,e). The Na-rich $\text{Na}_{3-\alpha}\text{V}_2(\text{PO}_4)_3$ phase and Na-poor $\text{Na}_\beta\text{V}_2(\text{PO}_4)_3$ phase are clearly observed in the operando XRD patterns. Obviously, the $\text{Na}_{3-\alpha}\text{V}_2(\text{PO}_4)_3$ peaks disappear on desodiation and are restored after the sodiation process. On the contrary, $\text{Na}_\beta\text{V}_2(\text{PO}_4)_3$ peaks form in the initial stage, and grow and disappear during the desodiation and sodiation processes, respectively. Moreover, the (211) and (300) peaks shift to

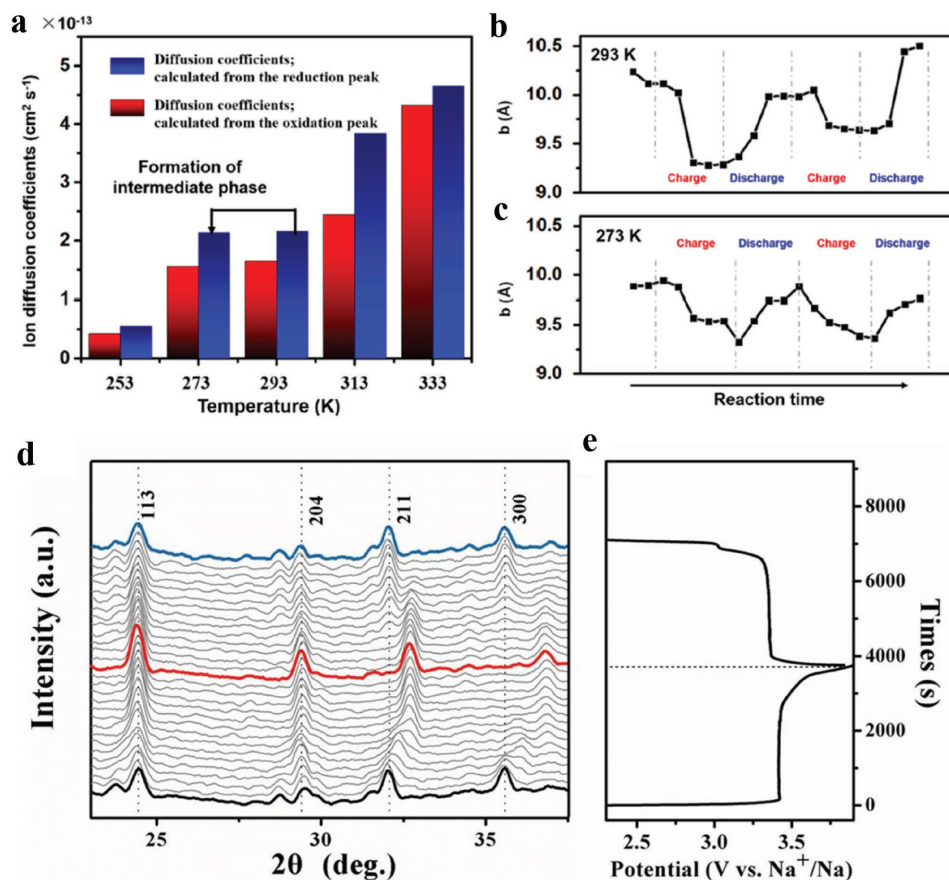


Figure 3. a) Ion-diffusion coefficients of LiFePO_4 at different temperatures. b,c) The unit cell parameter b as a function of reaction time, obtained from Rietveld refinement at temperatures of 293 K (b) and 273 K (c) with a scan rate of 1.4 mV s^{-1} . d) The operando XRD patterns of three-dimensional $\text{Na}_3\text{V}_2(\text{PO}_4)_3$ nanofiber network for a full charge/discharge cycle in a voltage range of 2.3–3.9 V. e) The corresponding time–potential curve. a–c) Reproduced with permission.^[27] Copyright 2016, Elsevier. d,e) Reproduced with permission.^[35] Copyright 2016, Elsevier.

higher angles during the desodiation process, indicating the d -spacings decrease during the extraction of the sodium ions. After fully charging, all of the peaks return to the original positions, manifesting the excellent structure reversibility.^[36] Therefore, the intrinsic sodium-storage mechanism and the reason for the excellent cycling stability of the $\text{Na}_3\text{V}_2(\text{PO}_4)_3$ are revealed by the operando XRD technique.

2.1.3. Investigating the Phase Transitions of $\text{LiMn}_{0.25}\text{Fe}_{0.75}\text{PO}_4$

As a lithium transition-metal phosphate, LiMnPO_4 is a good alternative to LiFePO_4 with a similar specific capacity (170 mA h g^{-1}) and a higher $\text{Mn}^{2+}/\text{Mn}^{3+}$ redox voltage (4.1 V vs Li^+/Li); however, its power capability is significantly reduced. To take advantage of LiFePO_4 and LiMnPO_4 , binary $\text{LiFe}_{1-x}\text{Mn}_x\text{PO}_4$ olivine cathodes have been studied by researchers.^[10] Chen et al.^[37] studied the phase transformations of $\text{LiMn}_{0.25}\text{Fe}_{0.75}\text{PO}_4$ during lithiation/delithiation using the operando XRD technique with synchrotron XRD. **Figure 4** shows the operando XRD patterns of $\text{Li}_x\text{Mn}_{0.25}\text{Fe}_{0.75}\text{PO}_4$ as a function of lithium content x during the first cycle (Figure 4a and Figure 4b showing respectively charge/discharge at 0.05C)

and second cycle (Figure 4c and Figure 4d showing respectively charge/discharge at 0.5C). It was observed that two significant two-phase transformations occur during delithiation. The first two-phase transformation is caused by an $\text{Fe}^{2+}/\text{Fe}^{3+}$ redox reaction. The $\text{Li}_x\text{Mn}_{0.25}^{2+}\text{Fe}_{0.75}^{3+}\text{PO}_4$ (020) peak begins to appear at $x = 0.62$, indicating the coexistence of $\text{Li}_x\text{Mn}_{0.25}^{2+}\text{Fe}_{0.75}^{2+}\text{PO}_4$ and $\text{Li}_x\text{Mn}_{0.25}^{2+}\text{Fe}_{0.75}^{3+}\text{PO}_4$. At $x = 0.30$, the phase becomes entirely $\text{Li}_x\text{Mn}_{0.25}^{2+}\text{Fe}_{0.75}^{3+}\text{PO}_4$. The second two-phase transformation is a result of the $\text{Mn}^{2+}/\text{Mn}^{3+}$ redox reaction. At $x = 0.14$, the $\text{Li}_x\text{Mn}_{0.25}^{3+}\text{Fe}_{0.75}^{3+}\text{PO}_4$ (020) peak begins to appear and the phase changes to $\text{Li}_x\text{Mn}_{0.25}^{3+}\text{Fe}_{0.75}^{3+}\text{PO}_4$ at $x = 0.02$. During the lithiation process, the two-phase transformation of the $\text{Mn}^{2+}/\text{Mn}^{3+}$ redox reaction still exists, but only the single-phase transformation of the $\text{Fe}^{2+}/\text{Fe}^{3+}$ redox reaction can be detected.

2.2. Layered Oxides

2.2.1. Investigating the Phase Transformations of $\text{V}_2\text{O}_5/\text{NaV}_6\text{O}_{15}$

Sodium-intercalated layered-oxides are another kind of promising cathode materials in rechargeable batteries. These layered-oxides can be categorized into three main groups according to

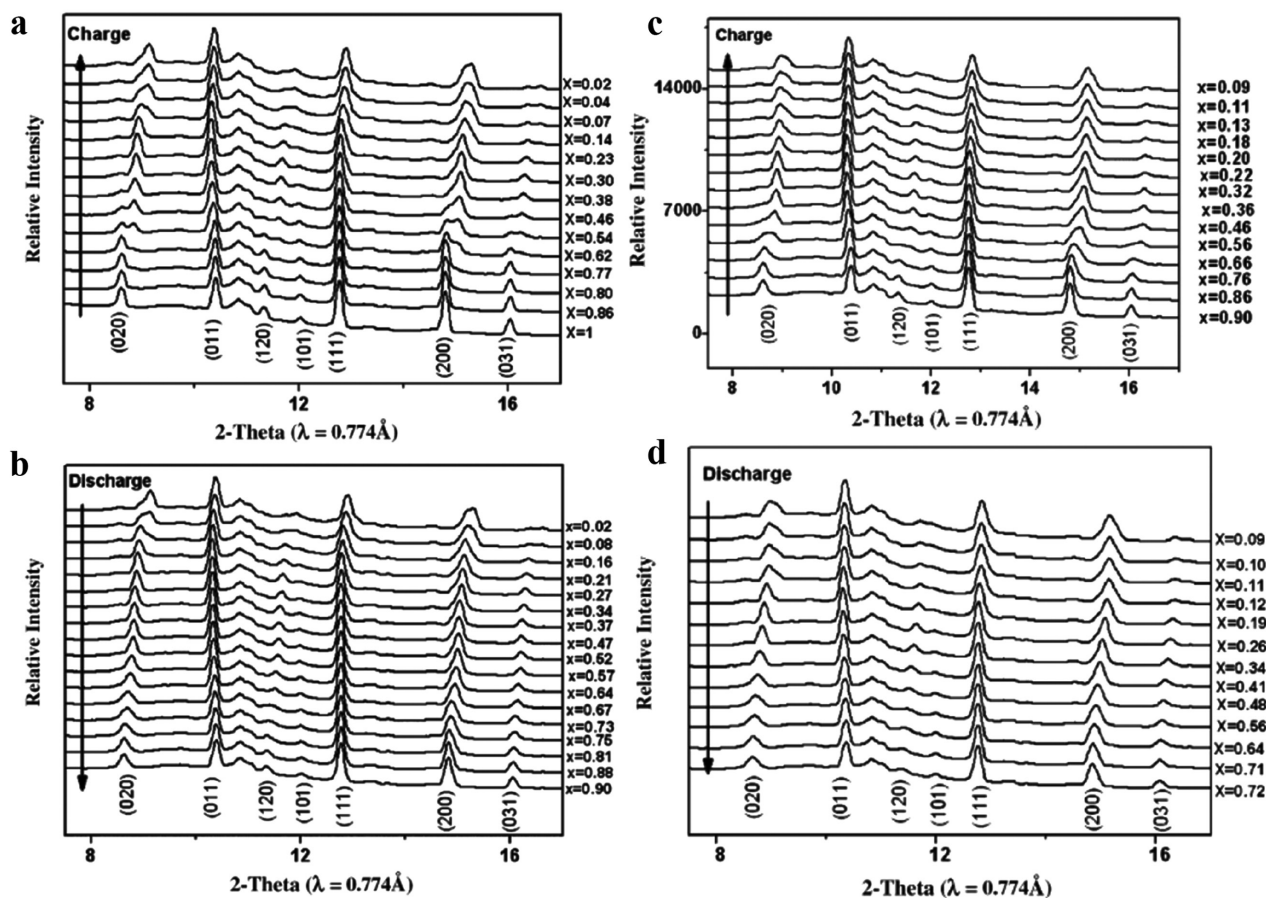


Figure 4. The operando XRD patterns of $\text{Li}_x\text{Mn}_{0.25}\text{Fe}_{0.75}\text{PO}_4$ as a function of the lithium content x during the first cycle (charge/discharge at 0.05C (a,b)) and second cycle (charge/discharge at 0.5C (c,d)). a–d) Reproduced with permission.^[37] Copyright 2009, Elsevier.

the freedom of the sodium ions (unable, partial, and complete insertion/extraction) in the crystal skeleton.^[38] These layered oxides are being revisited as cathode materials in LIBs/SIBs, due to their high theoretical capacity, low cost, and facile synthesis conditions.^[39–41] Among the different layered-oxides, vanadium-based layered-oxides are remarkably attractive candidates for rechargeable-battery cathodes due to their abundant resources, stable thermodynamic properties, and easy preparation.^[42,43] However, their poor rate capacity and low cycling stability seriously limit their further application in energy-storage systems. In order to overcome these problems, many scientists have done a lot of research work in this field.^[41–44] Niu et al.^[44] designed and fabricated a three-dimensional hierarchical heterostructure, $\text{V}_2\text{O}_5/\text{NaV}_6\text{O}_{15}$. The phase transformations of $\text{V}_2\text{O}_5/\text{NaV}_6\text{O}_{15}$ during the charge/discharge process were investigated by operando XRD with laboratory X-ray diffraction (Figure 5a–g). During the lithiation process, six stages of phase transformations are observed and exhibited accurately with the extension of time. In stage I, no obvious peak evolution occurs, while only a slight phase transformation is evident between $\text{Li}_{1/18}\text{Na}_{1/3}\text{V}_2\text{O}_5$ and $\text{Na}_{1/3}\text{V}_2\text{O}_5$. In stage II and IV, the evolution of distinct peaks associated with the V_2O_5 phase occurs. The peak evolutions indicate the phase transformation from V_2O_5 to $\epsilon\text{-Li}_{0.5}\text{V}_2\text{O}_5$ (stage II) and from $\epsilon\text{-Li}_{0.5}\text{V}_2\text{O}_5$ to $\delta\text{-LiV}_2\text{O}_5$ (stage IV), respectively. The other stages correspond

to the stepwise phase transformation from $\text{Li}_{1/18}\text{Na}_{1/3}\text{V}_2\text{O}_5$ to $\text{LiNa}_{1/3}\text{V}_2\text{O}_5$. The obvious evolution of the lattice parameters clearly demonstrates a synergistic effect between the branched $\text{NaV}_6\text{O}_{15}$ and the V_2O_5 backbone of the three-dimensional $\text{V}_2\text{O}_5/\text{NaV}_6\text{O}_{15}$ hierarchical heterogeneous microspheres during the lithiation/delithiation process, which can efficiently improve the lithium-storage performance. These valuable results demonstrate the intrinsic lithium-storage mechanism of the three-dimensional $\text{V}_2\text{O}_5/\text{NaV}_6\text{O}_{15}$ hierarchical heterogeneous microspheres in LIBs.

2.2.2. Stable Crystal Framework and Enlarged Diffusion Channel of $\text{K}_{0.7}\text{Fe}_{0.5}\text{Mn}_{0.5}\text{O}_2$

Potassium-ion batteries (KIBs), as a new type of energy-storage device, faces a major challenge, which is the lack of stable materials to accommodate the intercalation of the large-size potassium ions.^[45] Sodium-containing Fe/Mn-based layered materials ($\text{Na}_{0.7}\text{Fe}_x\text{Mn}_{1-x}\text{O}_2$, $0 < x < 1$) demonstrate high specific capacities but show poor cycling performance due to their structural instability upon insertion/extraction of the large-sized ions.^[46] To reinforce the layered structure of the Fe-/Mn-based materials, Wang et al.^[47] reported potassium-containing Fe-/Mn-based layered oxide ($\text{K}_{0.7}\text{Fe}_{0.5}\text{Mn}_{0.5}\text{O}_2$) interconnected nanowires as a cathode

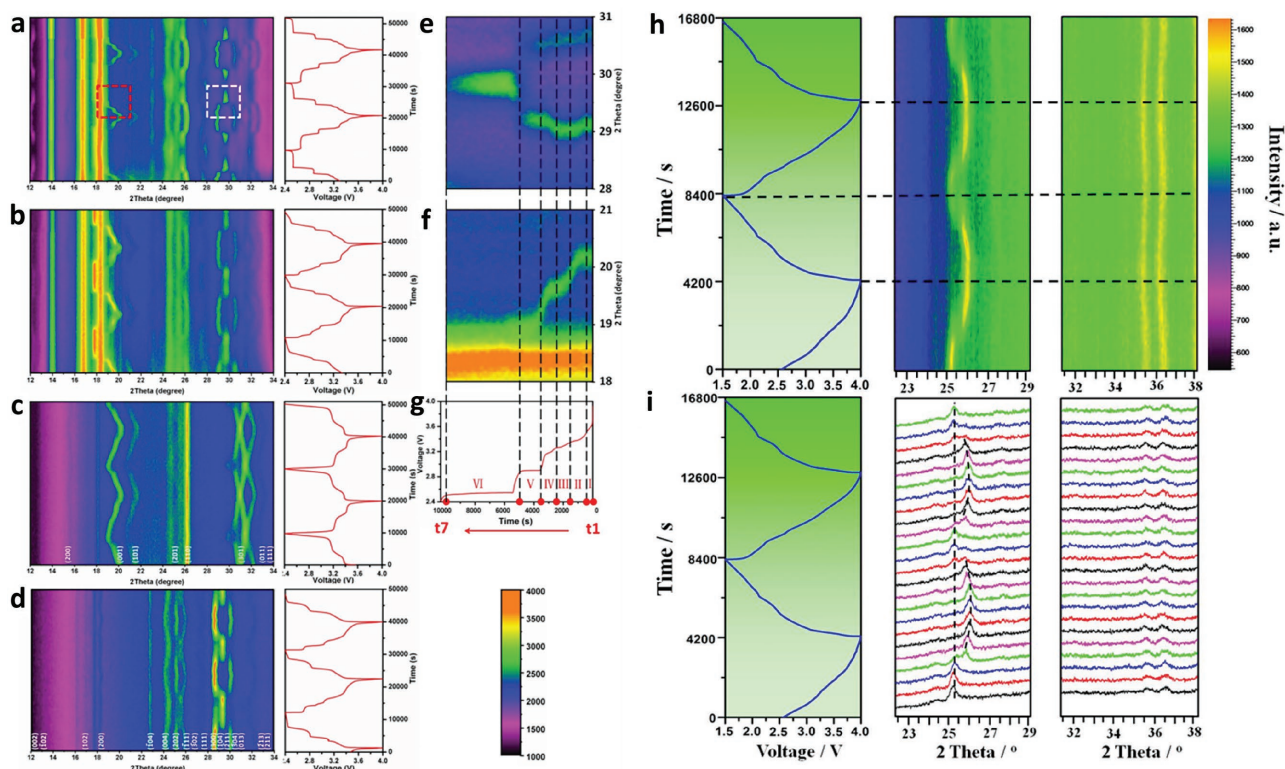


Figure 5. Operando X-ray diffraction patterns: a) 3D V_2O_5/NaV_6O_{15} hierarchical heterogeneous microspheres. b) V_2O_5/NaV_6O_{15} physical mixture. c) Pure V_2O_5 nanogears. d) Pure NaV_6O_{15} nanospindles. e–g) Magnified time-resolved evolution of 3D V_2O_5/NaV_6O_{15} hierarchical heterogeneous microspheres in one discharge process from 4.0 to 2.4 V. h) Operando XRD patterns of interconnected $K_{0.7}Fe_{0.5}Mn_{0.5}O_2$ nanowires at $22.5\text{--}29.0^\circ$ and $31.5\text{--}38.0^\circ$ during the first two cycles. i) The image plot of the XRD patterns at $22.3\text{--}29.2^\circ$ and $31.3\text{--}38.3^\circ$ during the first two cycles. a–g) Reproduced with permission.^[44] Copyright 2016, Elsevier. h,i) Reproduced with permission.^[47] Copyright 2016, American Chemical Society.

material for KIBs that exhibits both high capacity and good cycling stability. The structural evolutions of the $K_{0.7}Fe_{0.5}Mn_{0.5}O_2$ during the potassiation/depotassiation processes were characterized using the advanced operando XRD technique with laboratory XRD. No change was observed for the peak located at $2\theta = 25.2^\circ$ during the voltage increase from 3.27 to 3.7 V. However, one new peak appeared and was finally fixed at 26.0° when charging to 4.0 V. This trend was reversed during the first potassiation stage, indicating a reversible expansion/contraction. Another two peaks of 35.4° and 36.2° exhibited minor shifts to low angles at the end of depotassiation, and then returned to their original position during the potassiation. All the peaks were stably preserved or highly reversible during the potassiation/depotassiation processes apart from showing changes in their peak intensities (Figure 5h,i), confirming that $K_{0.7}Fe_{0.5}Mn_{0.5}O_2$ can provide a stable crystal framework.^[48,49] As a consequence, the highly reversible crystal structure of the interconnected $K_{0.7}Fe_{0.5}Mn_{0.5}O_2$ nanowires exhibits excellent potassium-storage performance for KIBs.

2.2.3. Studying the Phase Transformations of $P2-Na_xCoO_2$

Among sodium-intercalated layered-oxides, $P2-Na_xCoO_2$ attracts a high level of scientific interest given its unique physical properties due to the strong electronic correlations. Berthelot et al.^[50] identified a succession of single-phase or two-phase

domains appearing on sodium intercalation, combining the electrochemical process with the operando XRD technique and laboratory XRD. **Figure 6** shows the synergy between the electrochemistry and the operando XRD through sodium-ion intercalation in $P2-Na_xCoO_2$. The results of the operando XRD measurements indicate that the (008) diffraction peak was shifted to a higher 2θ position. It was proven that the interslab distance decreases during sodium intercalation. The (102) diffraction peak of the Be window is marked by the asterisk. A new $P2-Na_xCoO_2$ phase diagram is shown for the $\approx 0.62 \leq x < \approx 0.92$ region, exhibiting single-phase domains with either peculiar composition or solid-solution behavior, and biphasic domains.

3. Operando XRD Technique for Anode Materials

3.1. Anodes based on the Intercalation Reaction Mechanism

3.1.1. Investigation of the Sodium-Storage Mechanism in $Li_4Ti_5O_{12}$

Lithium titanium oxide spinel ($Li_4Ti_5O_{12}$) has been considered as one of the most promising anode materials for LIBs, due to its zero-strain insertion property, excellent structural stability, and high reversibility.^[51] However, $Li_4Ti_5O_{12}$ suffers from low electronic and ion conductivity, resulting in a high overpotential and a poor rate capability. To solve these issues, various work

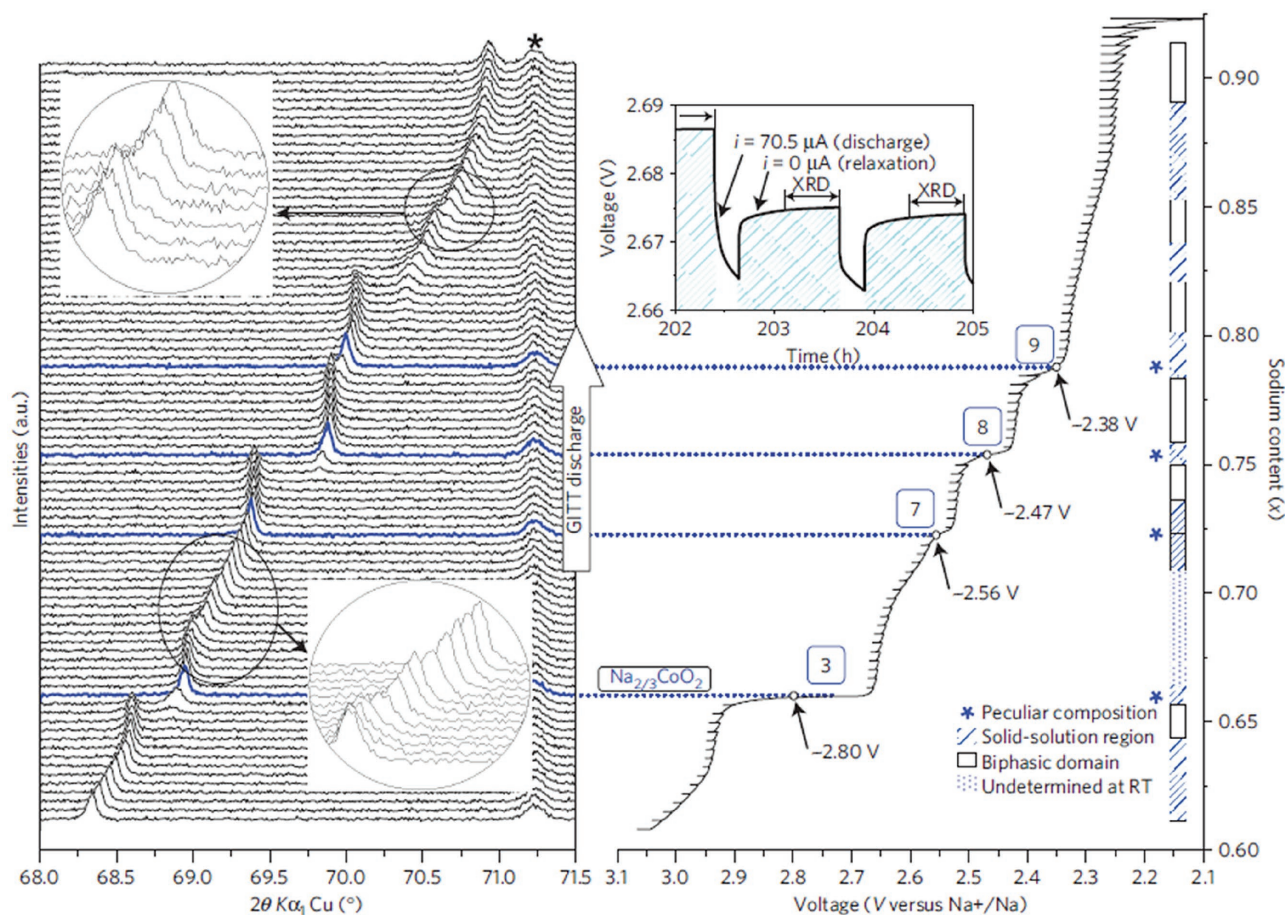


Figure 6. Synergy between electrochemistry and operando XRD through sodium-ion intercalation in P2- Na_xCoO_2 . The galvanostatic intermittent titration technique (GITT) electrochemical battery discharge (right side) enables the equilibrium potential for each given composition to be obtained. At the end of each relaxation step (top right inset), the operando XRD measurements (left side) are carried out to characterize the corresponding system. Reproduced with permission.^[50] Copyright 2011, Nature Publishing Group.

has focused on surface coating,^[52] doping with metal ions,^[53] and reducing the size of the electrode materials.^[54] Some nanostructured $\text{Li}_4\text{Ti}_5\text{O}_{12}$ materials have been developed to shorten the diffusion path of both electrons and ions, improving the electrochemical performance of the electrodes. Recently, $\text{Li}_4\text{Ti}_5\text{O}_{12}$ has also been reported as an anode material for SIBs, showing an average voltage of about 0.9 V.^[55] The relatively high storage voltage makes it much safer than hard carbon as an anode material. Zhao et al.^[56] adopted ex situ XRD to investigate for the first time the structure changes of $\text{Li}_4\text{Ti}_5\text{O}_{12}$ after sodium-ion insertion/extraction. However, the relationship between the structural changes and the electrochemical performance of the electrodes is far from clearly understood, which deserves more investigation via operando methods.^[57,58]

Sun et al.^[55] investigated the sodium-insertion mechanism of $\text{Li}_4\text{Ti}_5\text{O}_{12}$ via operando synchrotron XRD. These data were collected at Beamline BL148 ($\lambda = 0.12398$ nm) of the Synchrotron Radiation Facility, using an image plate detector in transmission mode. Mylar film was used as a window to allow the penetration of the synchrotron beam into the in situ cell. **Figure 7a** shows the operando synchrotron XRD results of the $\text{Li}_4\text{Ti}_5\text{O}_{12}$ electrode in the SIB system during the first charge/discharge process. During

the discharge process, new peaks of the Na_6Li phase appear. However, these peaks disappear in the following charging process, which indicate a phase-separation reaction instead of a solid-solution reaction occurring in the $\text{Li}_4\text{Ti}_5\text{O}_{12}$ electrode. Yu et al.^[54] studied the structure changes of a $\text{Li}_4\text{Ti}_5\text{O}_{12}$ electrode using a combination of chemical sodiation and operando XRD with synchrotron XRD. The result demonstrated that the sodium-storage behavior is size dependent. The XRD patterns of $\text{Li}_4\text{Ti}_5\text{O}_{12}$ (44 nm) during the chemical sodiation process are collected in **Figure 7b**. With increasing reaction time, the new peaks appear on the left side of the $\text{Li}_4\text{Ti}_5\text{O}_{12}$ (400) and (440). When the reaction time increases to 2 h, the sodiation process is complete, with no change of the XRD patterns. **Figure 7c** shows the XRD pattern of the final sodiated product, which confirms two new phases, $\text{Na}_6(16c)\text{LiTi}_5(16d)\text{O}_{12}(32e)$ and $\text{Li}_7\text{Ti}_5\text{O}_{12}$, were formed during sodium insertion. To further investigate the size effect on the phase-transition behavior, the XRD-pattern changes of the $\text{Li}_4\text{Ti}_5\text{O}_{12}$ samples with larger particle size (120 and 440 nm) were also studied during an operando chemical sodiation process (**Figure 7d–f**). Interestingly, the sodiation reaction does not complete until the reaction time increases to 24 h for $\text{Li}_4\text{Ti}_5\text{O}_{12}$ with a particle size of 120 nm. For 440 nm $\text{Li}_4\text{Ti}_5\text{O}_{12}$, no new

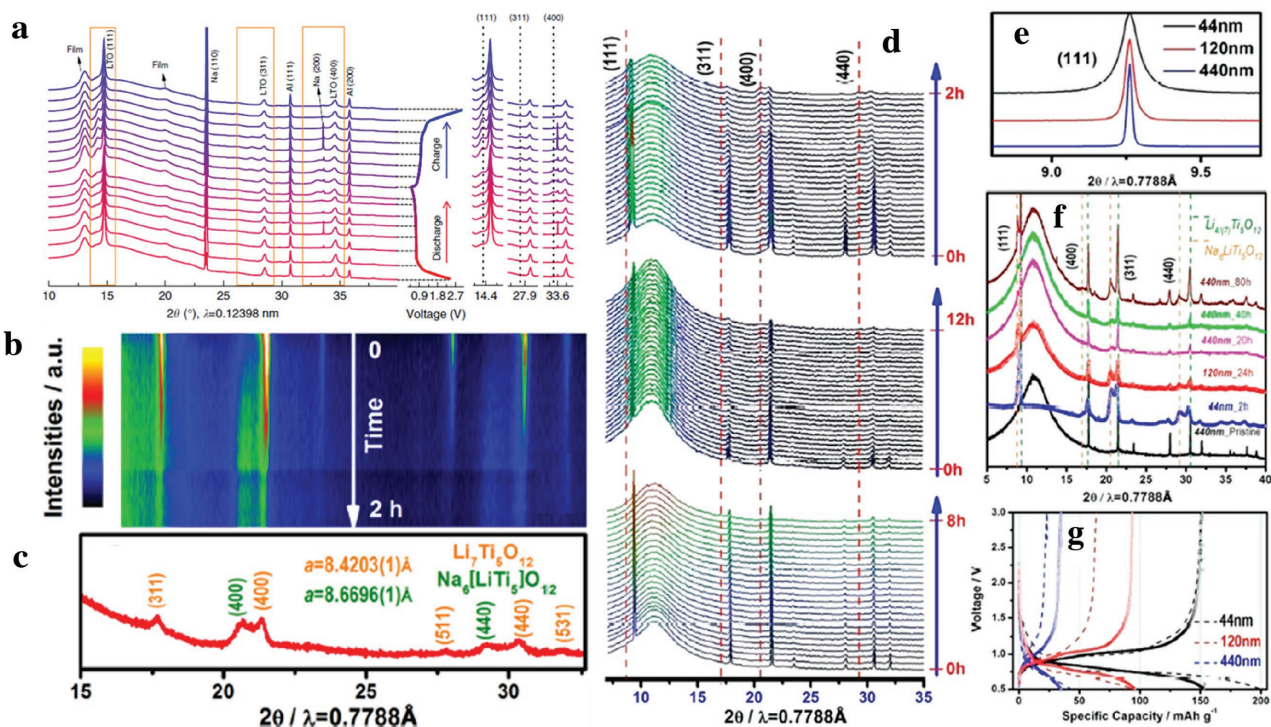


Figure 7. a) Operando synchrotron XRD patterns of $\text{Li}_4\text{Ti}_5\text{O}_{12}$ electrode in SIB system during the first cycle. b,c) XRD patterns of $\text{Li}_4\text{Ti}_5\text{O}_{12}$ (particle size ≈ 44 nm) during the chemical sodiation process and the final sodiated $\text{Li}_4\text{Ti}_5\text{O}_{12}$, respectively. d) Operando XRD patterns collected during chemical sodiation of the nanosized 44 nm (top), 120 nm (middle), and 440 nm (bottom) $\text{Li}_4\text{Ti}_5\text{O}_{12}$. e) Enlarged view of the (111) reflections for the pristine $\text{Li}_4\text{Ti}_5\text{O}_{12}$. f) XRD patterns of the sub-microsize $\text{Li}_4\text{Ti}_5\text{O}_{12}$ collected after chemical sodiation for 20, 40, and 80 h, respectively. g) The charge–discharge curve (first, dashed line; 30th, solid line) of sodium storage into $\text{Li}_4\text{Ti}_5\text{O}_{12}$ (0.1C, 0.5–3 V). a) Reproduced with permission.^[55] Copyright 2013, Nature Publishing Group. b–g) Reproduced with permission.^[54] Copyright 2013, American Chemical Society.

phase forms in the initial chemical sodiation stage (8 h). With the increase of the chemical sodiation time, the peaks of the $\text{Na}_6\text{LiTi}_5\text{O}_{12}$ phase appear and become stronger. However, only 36 wt% of the $\text{Li}_4\text{Ti}_5\text{O}_{12}$ is transformed to $\text{Na}_6\text{LiTi}_5\text{O}_{12}$ and $\text{Li}_7\text{Ti}_5\text{O}_{12}$ even after reaction for 80 h. The relationship between the sodium-storage performance and the particle size was also studied, as shown in Figure 7g. The specific capacity of 175 mA h g^{-1} was obtained after sodium insertion into $\text{Li}_4\text{Ti}_5\text{O}_{12}$ (44 nm), which is largely higher than that of 440 nm $\text{Li}_4\text{Ti}_5\text{O}_{12}$ (16 mA h g^{-1}). The results indicate that the sodium-storage performance of $\text{Li}_4\text{Ti}_5\text{O}_{12}$ is highly relevant to the particle size.

In summary, the advanced synchrotron-based operando XRD method was developed to investigate the phase-transition behavior of $\text{Li}_4\text{Ti}_5\text{O}_{12}$ as a SIB anode material. It has been demonstrated that the sodium-storage performance of $\text{Li}_4\text{Ti}_5\text{O}_{12}$ is related to the particle size. The operando XRD results provides a clear direction to improving the sodium-storage performance of $\text{Li}_4\text{Ti}_5\text{O}_{12}$, making it a suitable anode material for SIBs.

3.2. Anodes based on the Conversion Reaction Mechanism

3.2.1. Observation of the Electrochemical Reaction Process of Metal Oxides

Transition-metal oxides as conversion-type materials have been widely investigated for LIBs due to their high theoretical

capacity, relatively low cost, and environmental friendliness. However, these materials suffer from a large volume change and low conductivity during insertion/extraction of ions, hindering their practical applications. In order to circumvent these issues, various synthetic methods and operando analysis techniques have been developed to improve their performance and understand the electrochemical reaction mechanism. Lowe et al.^[59] studied the conversion-reaction mechanism of Mn_3O_4 anode material with operando synchrotron XRD and X-ray absorption spectra (XAS). The electrochemically induced variation of several intermediate phases during lithiation were probed. It was demonstrated that the Mn_3O_4 surfaces react first, with concurrent reduction of both Mn_3O_4 and LiMn_3O_4 throughout most of the higher-voltage regime. In addition, XAS results show that metallic Mn does not appear until the reduction of Mn^{2+} to an average oxidation state Mn^{1+} . Nanostructured metal-oxide materials have been synthesized, including nanosheets,^[60] nanowires,^[61] and nanotubes.^[62] Not only can the diffusion length be shortened, but also the volume expansion during insertion/extraction of ions can be accommodated. In addition, constructing hybrid electrodes composed of metal oxides and carbonaceous materials has also been proven as a facile and effective approach to enhance the electrochemical performance of anode materials.^[63] An et al.^[64] constructed amorphous matrices of vanadium oxides that supported hierarchical porous $\text{Fe}_3\text{O}_4/\text{graphene}$ nanowires ($\text{Fe}_3\text{O}_4/\text{VO}_x/\text{G-P}$ NWs) providing fast lithium-ion diffusion, effective electron

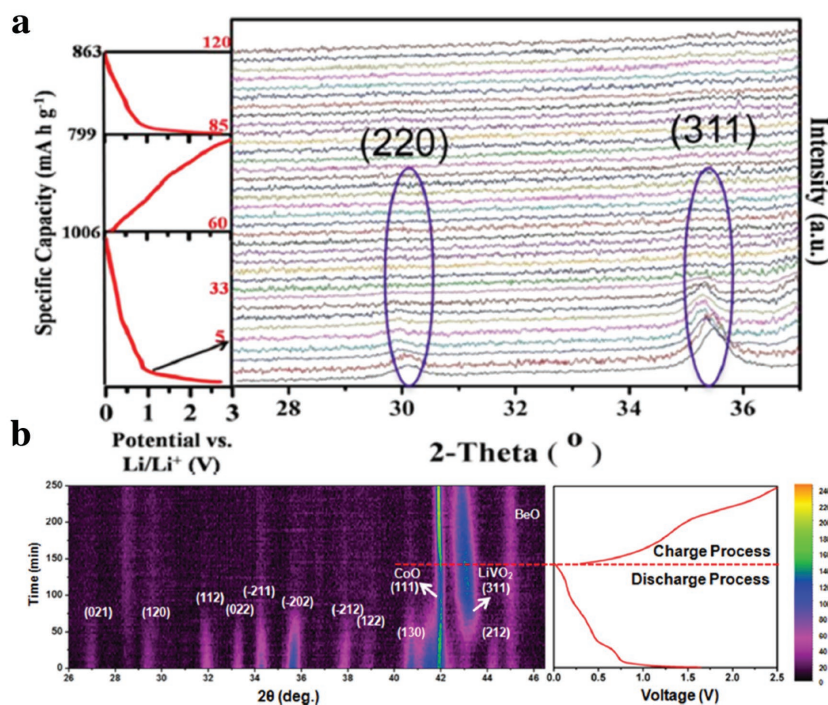


Figure 8. a) Operando XRD patterns of Fe₃O₄/VO_x/G-P nanowires. b) Operando XRD patterns of CoVO-1 (left) and corresponding discharge/charge curve (right). a) Reproduced with permission.^[64] Copyright 2014, American Chemical Society. b) Reproduced with permission.^[66] Copyright 2016, American Chemical Society.

transport, and excellent stress relaxation, exhibiting superior lithium-storage performance. The reaction mechanism of the Fe₃O₄/VO_x/G-P NWs was also investigated by operando XRD with laboratory XRD as shown in **Figure 8a**. During the first discharge process, it could be observed that the diffraction peaks of the (220) and (311) planes of Fe₃O₄ shift to a low angle, owing to the expansion of the electrode materials, while the two diffraction peaks become weaker and weaker until they completely disappear. There are no obvious diffraction peaks appearing during the following charge/discharge, indicating the formation of amorphous materials after lithium-ion insertion.

Recently, binary metal oxides have also been exploited as anode electrodes in LIBs, because they can synergistically enhance ion and electronic conductivity, mechanical stability, and reversible capacity.^[65] Luo et al.^[66] designed and synthesized hierarchical Co₂V₂O₇ nanosheets consisting of interconnected nanoparticles. They exhibited a high reversible specific capacity, excellent rate capability, and long cycle life, owing to the short pathways for ions/electrons and sufficient voids for the volume expansion. An operando XRD study with laboratory XRD was conducted to observe the reaction process of the hierarchical Co₂V₂O₇ nanosheets during cycling (Figure 8b). Three plateaus could be observed in the discharge curve. The peak intensity of the Co₂V₂O₇ just decreased and there were no other changes at the first plateau, which is associated with the formation of a solid electrolyte interface (SEI). However, the diffraction peaks of the Co₂V₂O₇ disappeared and a new peak formed at the second plateau. The new peak at 43° is indexed to the (311) diffraction peak of LiVO₂. On the basis of operando XRD characterization and CV measurement results, the electrochemical reaction mechanism of the Co₂V₂O₇

was revealed. Metallic Co and Li_{1+x}VO₂ formed in the initial discharge process. The formation of CoO from metallic Co and the delithiation of the vanadium oxides occurred in the subsequent charging process. In the following cycles, electrochemical reaction process corresponds to a reversible transformation reaction between the phases of CoO and Co.

3.3. Anodes based on the Alloying Reaction Mechanism

3.3.1. Investigation on the (De-)Lithiation Mechanism in Silicon

Silicon (Si) is widely considered as one of the most promising anode materials for LIBs due to its high theoretical capacity and abundant resources. However, the practical application of Si is limited by the large volume changes during the lithiation/delithiation processes. The large volume expansion causes the pulverization and cracking of Si, resulting in damage to the electrode, an unstable SEI, and limited cycle life.^[67–69] Various approaches have been developed to address these problems, such as designing pomegranate-like Si structures^[70] and nonfilling carbon-coated porous

Si microparticle core-shell structures.^[71] The cycling stability of Si has been largely improved by these efficient strategies. However, studies focused on understanding the (de-)lithiation and degradation mechanisms of Si anode material are still needed to further enhance its electrochemical properties. Despite the (de-)lithiation mechanisms of Si nanowires having been studied via ex situ XRD,^[72] they are still unclear in clarifying the real electrochemical reaction processes. Misra et al.^[73] investigated the lithium-ion insertion/extraction mechanism in Si-nanowire anodes by operando synchrotron XRD. The metastable Li₁₅Si₄ phase was observed at low potentials. Moreover, it was demonstrated that the existence of the crystalline phase degrades the cycling stability of Si. **Figure 9a–g** show the operando XRD results for Si on a stainless-steel mesh cell during the first and second lithiation/delithiation cycles. When the Si nanowires are lithiated, the diffraction peak intensity of Si(111) decreases, indicating the disappearance of crystalline Si and the formation of amorphous Li_xS (Figure 9c). The diffraction peaks corresponding to the Li₁₅Si₄ phase are observed at low potentials (<20 mV), which is consistent with previous studies on Si anode materials using operando methods.^[74] However, it is not possible to observe the presence of the Li₁₅Si₄ phase by ex situ studies. The results demonstrate the importance of operando techniques in probing the electrochemical reaction mechanism of electrodes.

3.3.2. Studying the Electrochemical Reaction Mechanism of Antimony

Antimony (Sb) has been widely investigated as an anode material for SIBs due to its low cost, environmental benignity, good

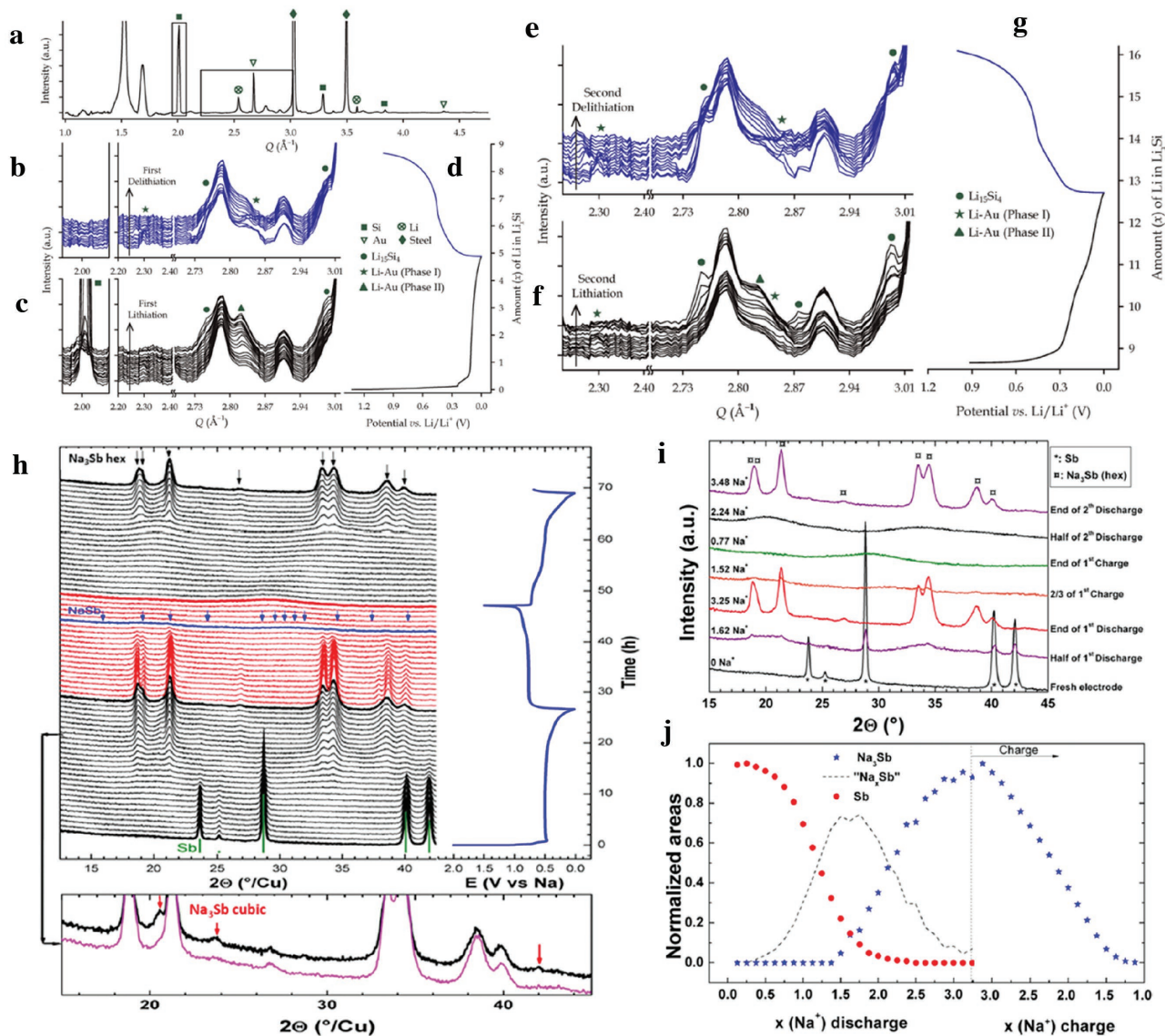


Figure 9. a–g) Operando XRD pattern for an stainless-steel (SS) mesh cell: a) at the start of the lithiation cycle; b–f) zoomed-in sections of Q -space regions shown in (a) for the first and second delithiation/lithiation cycles, respectively. d, g) Voltage profile showing the first and second cycles, respectively. h) Operando evolution of the XRD pattern recorded at a C/8 rate (top left). A zoom-in illustrating the diffraction peaks from the cubic Na_3Sb (bottom). i) Selected operando XRD patterns at various stages of discharge and charge of an Sb/Na cell. j) Normalized areas under the most intense diffraction peaks for Sb (28.8°) (in red) and Na_3Sb (21.2°) (in blue) during the first cycle plotted as a function of Na number (x). a–g) Reproduced with permission.^[73] Copyright 2012, American Chemical Society. h–j) Reproduced with permission.^[78] Copyright 2012, American Chemical Society.

electronic conductivity, and high theoretical capacity.^[75] Liang et al.^[76] reported Sb-nanorod arrays as an SIB anode material, exhibiting a high capacity of 620 mA h g^{-1} . Luo et al.^[77] fabricated Sb nanoparticles anchored in a three-dimensional carbon network, showing a high reversible sodium-storage capacity and stable cycling performance. To better understand the electrochemical reaction mechanism of Sb, Darwiche et al.^[78] investigated the phase-transformation process of bulk Sb in the first two cycles by operando XRD with laboratory XRD (Figure 9h–j). The diffraction-peak intensities of crystalline Sb decreased during the first discharge process. Peaks due to hexagonal Na_3Sb appear only after the Sb diffraction peaks vanish. New small peaks

corresponding to the cubic Na_3Sb can also be observed. The phase is completely amorphous at the end of the charge process. The results demonstrate that the Sb first transforms to an intermediate amorphous phase, Na_xSb , and then converts to cubic-hexagonal Na_3Sb mixed phases, finally stabilizing as the hexagonal Na_3Sb phase during the discharge process. On the contrary, the Na_3Sb disappears and the amorphous Sb and Na_xSb phase occur during the charge process. The reversible electrochemical mechanism occurs between two phases through an amorphous intermediate phase. The existence of the intermediate amorphous phase can relieve strain, explaining the enhanced cycling performance of Sb as an SIB anode material.

4. Conclusion and Perspective

The physical and chemical changes in electrode materials are important factors that affect the electrochemical properties of electrodes. Detecting their electrochemical-reaction mechanism and phase-transformation process during cycling is meaningful to achieve high-performance electrode materials. Operando analytic techniques have been developed to observe the electrochemical reaction process of electrodes under working conditions. The operando XRD technique, as an important analytic tool, can efficiently probe the phase transitions and crystal-structure evolution in electrodes, which is useful for designing next-generation electrode materials for rechargeable batteries.

Here, we have summarized the recent advances in studying the electrochemical reaction process of electrodes during charge/discharge processes by operando XRD analysis method. By understanding the real-time chemical changes, as well as the physical changes in electrodes, including the evolution of the phase-transformation reaction and the formation of an intermediate phase during cycling, we can realize and design better electrode materials for rechargeable batteries. Although great progress in the development of the operando XRD method has been made for studying LIBs and SIBs, it remains a challenge to monitor the complex electrochemical process in a metal-air, multivalent-ion battery system. In addition, it is also difficult to detect low-crystallinity samples and achieve detailed information in a certain area. Pushing the development and improvements of the operando XRD technique is very important for achieving high-performance rechargeable batteries. One way is to improve and enhance the light-source intensity and detection precision. An enhanced X-ray intensity can efficiently improve the precision of the detection, but an ultrahigh intensity may impart radiation damage to battery samples. To enhance the signal source intensity and avoid the damage of samples, we can control the X-ray intensity in an appropriate range and extend the detection time to achieve better measurement results. In addition, the combination of the operando XRD technique and other advanced operando techniques will also be a promising strategy to probe and trace the specific electrochemical changes in electrodes, which can provide considerable insight on the correlation between structure changes and electrochemical performance of electrode materials.

Acknowledgements

This work was supported by the National Key Research and Development Program of China (2016YFA0202603), the National Basic Research Program of China (2013CB934103), the Program of Introducing Talents of Discipline to Universities (B17034), the National Natural Science Foundation of China (51521001, 51602239), the National Natural Science Fund for Distinguished Young Scholars (51425204), the Hubei Provincial Natural Science Foundation of China (2016CFB267), and the Fundamental Research Funds for the Central Universities (WUT: 2016111001, 2016111003, 20161VA090, 2017111009, 2017111007). L.M. gratefully acknowledges financial support from the China Scholarship Council (No. 201606955096).

Conflict of Interest

The authors declare no conflict of interest.

Keywords

electrode materials, intrinsic mechanism, operando X-ray diffraction, rechargeable batteries

Received: January 18, 2017

Revised: March 9, 2017

Published online:

- [1] J. Yang, S. Muhammad, M. R. Jo, H. Kim, K. Song, D. A. Agyeman, Y. I. Kim, W. S. Yoon, Y. M. Kang, *Chem. Soc. Rev.* **2016**, *45*, 5717.
- [2] N. Yabuuchi, K. Kubota, M. Dahbi, S. Komaba, *Chem. Rev.* **2014**, *114*, 11636.
- [3] Y. L. Ding, Y. Wen, C. Wu, P. A. van Aken, J. Maier, Y. Yu, *Nano Lett.* **2015**, *15*, 1388.
- [4] C. Chen, Y. Wen, X. Hu, X. Ji, M. Yan, L. Mai, P. Hu, B. Shan, Y. Huang, *Nat. Commun.* **2015**, *6*, 6929.
- [5] Y. J. Li, J. M. Fan, M. S. Zheng, Q. F. Dong, *Energy Environ. Sci.* **2016**, *9*, 1998.
- [6] K. T. Kim, C. Y. Yu, C. S. Yoon, S. J. Kim, Y. K. Sun, S. T. Myung, *Nano Energy* **2015**, *12*, 725.
- [7] H. Gwon, D. H. Seo, S. W. Kim, J. Kim, K. Kang, *Adv. Funct. Mater.* **2009**, *19*, 3285.
- [8] X. J. Wei, C. J. Tang, X. P. Wang, L. Zhou, Q. L. Wei, M. Y. Yan, J. Z. Sheng, P. Hu, B. L. Wang, L. Q. Mai, *ACS Appl. Mater. Interfaces* **2015**, *7*, 26572.
- [9] Y. Sharma, N. Sharma, G. V. Subba Rao, B. V. R. Chowdari, *Adv. Funct. Mater.* **2007**, *17*, 2855.
- [10] J. Kim, K. Y. Park, I. Park, J. K. Yoo, J. Hong, K. Kang, *J. Mater. Chem.* **2012**, *22*, 11964.
- [11] Y. L. Zhao, J. G. Feng, X. Liu, F. C. Wang, L. F. Wang, C. W. Shi, L. Huang, X. Feng, X. Y. Chen, L. Xu, M. Y. Yan, Q. J. Zhang, X. D. Bai, H. A. Wu, L. Q. Mai, *Nat. Commun.* **2014**, *5*, 4565.
- [12] X. Hua, R. Robert, L. S. Du, K. M. Wiaderek, M. Leskes, K. W. Chapman, P. J. Chupas, C. P. Grey, *J. Phys. Chem. C* **2014**, *118*, 15169.
- [13] L. Q. Mai, Y. J. Dong, L. Xu, C. H. Han, *Nano Lett.* **2010**, *10*, 4273.
- [14] J. Lee, D. H. Seo, M. Balasubramanian, N. Twu, X. Li, G. Ceder, *Energy Environ. Sci.* **2015**, *8*, 3255.
- [15] J. Nelson, S. Misra, Y. Yang, A. Jackson, Y. Liu, H. Wang, H. Dai, J. C. Andrews, Y. Cui, M. F. Toney, *J. Am. Chem. Soc.* **2012**, *134*, 6337.
- [16] D. Wu, X. Li, B. Xu, N. Twu, L. Liu, G. Ceder, *Energy Environ. Sci.* **2015**, *8*, 195.
- [17] L. Wang, J. Wang, X. Zhang, Y. Ren, R. Zuo, G. Yin, J. Wang, *Nano Energy* **2017**, *34*, 215.
- [18] A. K. Padhi, K. S. Nanjundaswamy, J. B. Goodenough, *J. Electrochem. Soc.* **1997**, *144*, 1188.
- [19] J. Wang, X. Sun, *Energy Environ. Sci.* **2015**, *8*, 1110.
- [20] C. Delmas, M. Maccario, L. Croguennec, F. Le Cras, F. Weill, *Nat. Mater.* **2008**, *7*, 665.
- [21] Y. Orikasa, T. Maeda, Y. Koyama, H. Murayama, K. Fukuda, H. Tanida, H. Arai, E. Matsubara, Y. Uchimoto, Z. Ogumi, *Chem. Mater.* **2013**, *25*, 1032.
- [22] I. Takahashi, T. Mori, T. Yoshinari, Y. Orikasa, Y. Koyama, H. Murayama, K. Fukuda, M. Hatano, H. Arai, Y. Uchimoto, T. Terai, *J. Power Sources* **2016**, *309*, 122.
- [23] C. Nan, J. Lu, L. Li, L. Li, Q. Peng, Y. Li, *Nano Res.* **2013**, *6*, 469.
- [24] X. L. Wu, Y. G. Guo, J. Su, J. W. Xiong, Y. L. Zhang, L. J. Wan, *Adv. Energy Mater.* **2013**, *3*, 1155.

- [25] Y. Orikasa, T. Maeda, Y. Koyama, H. Murayama, K. Fukuda, H. Tanida, H. Arai, E. Matsubara, Y. Uchimoto, Z. Ogumi, *J. Am. Chem. Soc.* **2013**, *135*, 5497.
- [26] H. Liu, F. C. Strobridge, O. J. Borkiewicz, K. M. Wiaderek, K. W. Chapman, P. J. Chupas, C. P. Grey, *Science* **2014**, *344*, 1252817.
- [27] M. Y. Yan, G. B. Zhang, Q. L. Wei, X. C. Tian, K. N. Zhao, Q. Y. An, L. Zhou, Y. L. Zhao, C. J. Niu, W. H. Ren, L. He, L. Q. Mai, *Nano Energy* **2016**, *22*, 406.
- [28] Z. Jian, W. Han, X. Lu, H. Yang, Y. Hu, J. Zhou, Z. Zhou, J. Li, W. Chen, D. Chen, L. Chen, *Adv. Energy Mater.* **2013**, *3*, 156.
- [29] Y. Fang, L. Xiao, X. Ai, Y. Cao, H. Yang, *Adv. Mater.* **2015**, *27*, 5895.
- [30] C. Xu, Y. N. Xu, C. J. Tang, Q. L. Wei, J. S. Meng, L. Huang, L. Zhou, G. B. Zhang, L. He, L. Q. Mai, *Nano Energy* **2016**, *28*, 224.
- [31] M. Bianchini, F. Fauth, N. Brisset, F. Weill, E. Suard, C. Masquelier, L. Croguennec, *Chem. Mater.* **2015**, *27*, 3009.
- [32] H. Gao, Y. Li, K. Park, J. B. Goodenough, *Chem. Mater.* **2016**, *28*, 6553.
- [33] C. Zhu, K. Song, P. A. van Aken, J. Maier, Y. Yu, *Nano Lett.* **2014**, *14*, 2175.
- [34] J. N. Chotard, G. Rousse, R. David, O. Mentre, M. Courty, C. Masquelier, *Chem. Mater.* **2015**, *27*, 5982.
- [35] W. H. Ren, Z. P. Zheng, C. Xu, C. J. Niu, Q. L. Wei, Q. Y. An, K. N. Zhao, M. Y. Yan, M. S. Qin, L. Q. Mai, *Nano Energy* **2016**, *25*, 145.
- [36] X. P. Wang, C. J. Niu, J. S. Meng, P. Hu, X. M. Xu, X. J. Wei, L. Zhou, K. N. Zhao, W. Luo, M. Y. Yan, L. Q. Mai, *Adv. Energy Mater.* **2015**, *5*, 1500716.
- [37] Y. C. Chen, J. M. Chen, C. H. Hsu, J. W. Yeh, H. C. Shih, Y. S. Chang, H. S. Sheu, *J. Power Sources* **2009**, *189*, 790.
- [38] N. Yabuuchi, M. Kajiyama, J. Iwatate, H. Nishikawa, S. Hitomi, R. Okuyama, R. Usui, Y. Yamada, S. Komaba, *Nat. Mater.* **2012**, *11*, 512.
- [39] D. Kim, S. H. Kang, M. Slater, S. Rood, J. T. Vaughey, N. Karan, M. Balasubramanian, C. S. Johnson, *Adv. Energy Mater.* **2011**, *1*, 333.
- [40] M. H. Han, E. Gonzalo, G. Singh, T. Rojo, *Energy Environ. Sci.* **2015**, *8*, 81.
- [41] S. M. Oh, S. T. Myung, C. S. Yoon, J. Lu, J. Hassoun, B. Scrosati, K. Amine, Y. K. Sun, *Nano Lett.* **2014**, *14*, 1620.
- [42] M. Guignard, C. Didier, J. Darriet, P. Bordet, E. Elkaïm, C. Delmas, *Nat. Mater.* **2013**, *12*, 74.
- [43] X. J. Wei, Q. Y. An, Q. L. Wei, M. Y. Yan, X. P. Wang, Q. D. Li, P. F. Zhang, B. L. Wang, L. Q. Mai, *Phys. Chem. Chem. Phys.* **2014**, *16*, 18680.
- [44] C. J. Niu, X. Liu, J. S. Meng, L. Xu, M. Y. Yan, X. P. Wang, G. B. Zhang, Z. A. Liu, X. M. Xu, L. Q. Mai, *Nano Energy* **2016**, *27*, 147.
- [45] Z. Jian, W. Luo, X. Ji, *J. Am. Chem. Soc.* **2015**, *137*, 11566.
- [46] C. J. Niu, J. S. Meng, X. P. Wang, C. H. Han, M. Y. Yan, K. N. Zhao, X. M. Xu, W. H. Ren, Y. L. Zhao, L. Xu, Q. J. Zhang, D. Y. Zhao, L. Q. Mai, *Nat. Commun.* **2015**, *6*, 7402.
- [47] X. P. Wang, X. M. Xu, C. J. Niu, J. S. Meng, M. Huang, X. Liu, Z. A. Liu, L. Q. Mai, *Nano Lett.* **2017**, *1*, 544.
- [48] Y. Li, Z. Yang, S. Xu, L. Mu, L. Gu, Y. S. Hu, H. Li, L. Chen, *Adv. Sci.* **2015**, *2*, 1500031.
- [49] Y. Wang, R. Xiao, Y. S. Hu, M. Avdeev, L. Chen, *Nat. Commun.* **2015**, *6*, 6954.
- [50] R. Berthelot, D. Carlier, C. Delmas, *Nat. Mater.* **2011**, *10*, 74.
- [51] L. Shen, C. Yuan, H. Luo, X. Zhang, K. Xu, F. Zhang, *J. Mater. Chem.* **2011**, *21*, 761.
- [52] L. Zhao, Y. S. Hu, H. Li, Z. Wang, L. Chen, *Adv. Mater.* **2011**, *23*, 1385.
- [53] H. Song, S. W. Yun, H. H. Chun, M. G. Kim, K. Y. Chung, H. S. Kim, B. W. Cho, Y. T. Kim, *Energy Environ. Sci.* **2012**, *5*, 9903.
- [54] X. Yu, H. Pan, W. Wan, C. Ma, J. Bai, Q. Meng, S. N. Ehrlich, Y. S. Hu, X. Q. Yang, *Nano Lett.* **2013**, *13*, 4721.
- [55] Y. Sun, L. Zhao, H. Pan, X. Lu, L. Gu, Y. S. Hu, H. Li, M. Armand, Y. Ikuhara, L. Chen, X. Huang, *Nat. Commun.* **2013**, *4*, 1870.
- [56] L. Zhao, H. L. Pan, Y. S. Hu, H. Li, L. Q. Chen, *Chin. Phys. B* **2012**, *21*, 028201.
- [57] G. Du, N. Sharma, V. K. Peterson, J. A. Kimpton, D. Jia, Z. Guo, *Adv. Funct. Mater.* **2011**, *21*, 3990.
- [58] W. K. Pang, V. K. Peterson, N. Sharma, J. J. Shiu, S. H. Wu, *Chem. Mater.* **2014**, *26*, 2318.
- [59] M. A. Lowe, J. Gao, H. D. Abruña, *J. Mater. Chem. A* **2013**, *1*, 2094.
- [60] J. Zhu, Z. Yin, D. Yang, T. Sun, H. Yu, H. E. Hoster, H. H. Hng, H. Zhang, Q. Yan, *Energy Environ. Sci.* **2013**, *6*, 987.
- [61] M. S. Park, G. X. Wang, Y. M. Kang, D. Wexler, S. X. Dou, H. K. Liu, *Angew. Chem. Int. Ed.* **2007**, *119*, 764.
- [62] X. W. Lou, D. Deng, J. Y. Lee, J. Feng, L. A. Archer, *Adv. Mater.* **2008**, *20*, 258.
- [63] C. He, S. Wu, N. Zhao, C. Shi, E. Liu, J. Li, *ACS Nano* **2013**, *7*, 4459.
- [64] Q. Y. An, F. Lv, Q. Q. Liu, C. H. Han, K. N. Zhao, J. Z. Sheng, Q. L. Wei, M. Y. Yan, L. Q. Mai, *Nano Lett.* **2014**, *14*, 6250.
- [65] G. Yang, H. Cui, G. Yang, C. Wang, *ACS Nano* **2014**, *8*, 4474.
- [66] Y. Z. Luo, X. Xu, Y. X. Zhang, C. Y. Chen, L. Zhou, M. Y. Yan, Q. L. Wei, X. C. Tian, L. Q. Mai, *ACS Appl. Mater. Interfaces* **2016**, *8*, 2812.
- [67] D. Lin, Z. Lu, P. C. Hsu, H. R. Lee, N. Liu, J. Zhao, H. Wang, C. Liu, Y. Cui, *Energy Environ. Sci.* **2015**, *8*, 2371.
- [68] Y. S. Hu, R. Demir-Cakan, M. M. Titirici, J. O. Müller, R. Schlögl, M. Antonietti, J. Maier, *Angew. Chem. Int. Ed.* **2008**, *47*, 1645.
- [69] J. Deng, H. Ji, C. Yan, J. Zhang, W. Si, S. Baunack, S. Oswald, Y. Mei, O. G. Schmidt, *Angew. Chem. Int. Ed.* **2013**, *52*, 2326.
- [70] N. Liu, Z. Lu, J. Zhao, M. T. McDowell, H. W. Lee, W. Zhao, Y. Cui, *Nat. Nanotechnol.* **2014**, *9*, 187.
- [71] Z. Lu, N. Liu, H. W. Lee, J. Zhao, W. Li, Y. Li, Y. Cui, *ACS Nano* **2015**, *9*, 2540.
- [72] C. K. Chan, H. Peng, G. Liu, K. McIlwrath, X. F. Zhang, R. A. Huggins, Y. Cui, *Nat. Nanotechnol.* **2008**, *3*, 31.
- [73] S. Misra, N. Liu, J. Nelson, S. S. Hong, Y. Cui, M. F. Toney, *ACS Nano* **2012**, *6*, 5465.
- [74] T. D. Hatchard, J. R. Dahn, *J. Electrochem. Soc.* **2004**, *151*, A838.
- [75] Y. Zhu, X. Han, Y. Xu, Y. Liu, S. Zheng, K. Xu, L. Hu, C. Wang, *ACS Nano* **2013**, *7*, 6378.
- [76] L. Liang, Y. Xu, C. Wang, L. Wen, Y. Fang, Y. Mi, M. Zhou, H. Zhao, Y. Lei, *Energy Environ. Sci.* **2015**, *8*, 2954.
- [77] W. Luo, P. F. Zhang, X. P. Wang, Q. D. Li, Y. F. Dong, J. C. Hua, L. Zhou, L. Q. Mai, *J. Power Sources* **2016**, *304*, 340.
- [78] A. Darwiche, C. Marino, M. T. Sougrati, B. Fraisse, L. Stievano, L. Monconduit, *J. Am. Chem. Soc.* **2012**, *134*, 20805.